Ocean Engineering 232 (2021) 109019

Contents lists available at ScienceDirect

Ocean Engineering

journal homepage: www.elsevier.com/locate/oceaneng

ROV launch and recovery from an unmanned autonomous surface vessel – Hydrodynamic modelling and system integration

Chenyu Zhao [a,*], Philipp Thies [a], Johanning Lars [a,c], James Cowles [b]

[a] Renewable Energy Group, College of Engineering, Mathematics and Physical Sciences, University of Exeter, UK
[b] L3Harris Technologies, UK
[c] Naval Architecture, Harbin Engineering University, Nantong Main Street 145, Nangang District, Harbin, China

ARTICLE INFO

Keywords:
Unmanned vehicle system
Analytical model ROV
ASV
Numerical model
Winch

ABSTRACT

This paper focusses on the hydrodynamic performance of an unmanned vehicle system, consisting of a remotely operated underwater vehicle (ROV) that has to be launched and recovered autonomously from an Autonomous Surface Vehicles (ASV). The hydrodynamic model of the ASV/ROV coupled system is described in detail and solved numerically. The paper seeks to assess the overall performance of the ASV/ROV system, including the stability of the ASV, the ROV tidal current capacity and the required power of the launch and recovery winch system. The results demonstrate that this ASV/ROV system can complete the launch, holding and recovery tasks meeting stability for the given winch power requirements. The tidal current capacity of the ROV decreases with a larger target water depth. The maximum ROV umbilical tension is observed during steep wave instances when the ROV is in proximity to the ASV. A down-control force is demonstrated to be a suitable solution to limit the maximum tension within the umbilical rated force limits. This paper presents the methods and considerations for working towards a fully autonomous ASV/ROV system capable of autonomous inspection and maintenance missions. The work will be useful for practitioners and researcher working on autonomous offshore systems.

1. Introduction

In an effort to reduce both human risk exposure and cost, Unmanned Surface Vehicles (USVs) offer a possible practical solution. Generally, Autonomous vessels can be categorised into Autonomous Surface Vehicles (ASVs) and Remotely Operated underwater Vehicles (ROVs) (Kumar and Kurmi, 2018). The application areas of ASV have expanded into scientific research (Roberts and Sutton, 2006; Yan et al., 2010), environmental missions (Švec et al., 2014) and ocean resource exploration (Bertram, 2008; Pastore and Djapic, 2010). For example, a double-hull ASV was designed to perform river missions and estuarine scenarios, including bathymetry and environmental monitoring (Ferreira et al., 2007). A new ASV concept, operating in submerged conditions, was demonstrated in sea trials, successfully implementing larger payloads of 300 kg and a more flexible layout inside the vehicle (Sager et al., 2008).

ROVs are controlled through a crew or a remote system and are connected with a base station or a vessel by an umbilical which supplies the power and data signal connectivity (Christ and Wernli Sr, 2011). Considering their purpose, ROVs are categorised into inspection-class and intervention-class vehicles (Capocci et al., 2017). The intervention-class usually has a large mass (200 kg–5,000 kg) and can operate in very deep water (up to 6,000m) but are high cost. In most cases (shown in Table 1), the inspection-class ROV meets the mission requirements. The rated depth of this class device is usually less than 300m. Owing to its relatively smaller mass, the inspection-class ROV can be manually recovered (Bruno et al., 2015; Frost et al., 1996).

The challenge addressed by this work is to develop a genuinely autonomous couple between the ASV and the ROV. A range of different control methods has been devised and implemented, to support ROVs directly from an ASV autonomously. These methods include linear methods such as decoupled control (Healey and Marco, 1992), PID control (Healey and Lienard, 1993) Linear-Quadratic-Gaussian control (Field et al., 2000) and nonlinear methods like Sliding Mode Control (Cristi et al., 1990), adaptive control (Li and Lee, 2005).

In this work, ASV and ROV are connected by the launch and recovery system (LARS). The LARS is usually equipped with a tether management system (TMS). In (Trslic et al., 2020), the cage-type TMS with an ROV is translated by LARS as a heave motion. Other systems, such as (Conte et al., 2017), are designed without the docking station but are instead

* Corresponding author.
E-mail address: c.zhao@exeter.ac.uk (C. Zhao).

https://doi.org/10.1016/j.oceaneng.2021.109019
Received 15 December 2020; Received in revised form 6 April 2021; Accepted 10 April 2021
Available online 17 May 2021

Table 1
Cases applications for inspection-class ROVs (Capocci et al., 2017).

Applications	Cases
Environmental study	Coastal monitoring, Habitat monitoring, Pollution assessments, Hull inspections, unexploded (UXO) ordnance surveys, Contraband detection
Sciences	Seabed investigation, Marine life studies, Water and sediment sampling
Offshore oil and gas	Pipe and structure inspection, visual leak detection, Diver buddy operations
Marine renewable energy	Structure inspection

equipped with video ray micro-ROVs to launch and recover the ROV directly.

The coupled effects caused by the LARS operations could significantly influence the hydrodynamic performances of both ASV and ROV (Sivčev et al., 2018). However, in the available literature, the two systems are usually studied separately. For instance, Chin and Lau (2012) determined the hydrodynamic damping of a complex-shaped ROV by numerical and physical means. Eidsvik (2015) applies basic empirical coefficients to obtain the hydrodynamic parameters of the ROV, and this empirical method is tested on the five ROVs with different shapes. Compared with the experimental results, it was believed that the empirical method accurately evaluates the added mass of the ROV while slightly overestimating its radiation damping. Julca Avila et al. (2012) determined the Morison's equation inertia and drag coefficients of an ROV via a basin test. Alvarez et al. (2009) optimised the hydrodynamic performance of the ROV hull when it is near the water surface. The coupled effects between the umbilical and ROV are discussed in (Zhu et al., 2008), but the influences caused by the ASV are not explicitly accounted for. In their study, the ROV is regarded as a 6-DOF lumped buoy, the umbilical connected with the ROV has a constant length (300m) without any pay-out/in speed. Both physical and numerical results showed that the tidal current could significantly affect the umbilical tension.

This paper evaluates the hydrodynamic performance of an ASV/ROV system as well as its launch and recovery control strategy. A fully nonlinear numerical model based on the potential flow theory is employed to incorporate the coupled effects between the ASV, the ROV and the connecting umbilical. The paper is organised as follows: Section 2 lays out the analytical model of the ASV/ROV coupled system; Section 3 introduces the ASV system and the numerical model used in the case study; Section 4 presents the hydrodynamic performance results of the ASV/ROV system. Section 5 discusses the main findings in light of potential industrial applications and further R&D requirements. Section 6 concludes with the main findings and outcomes.

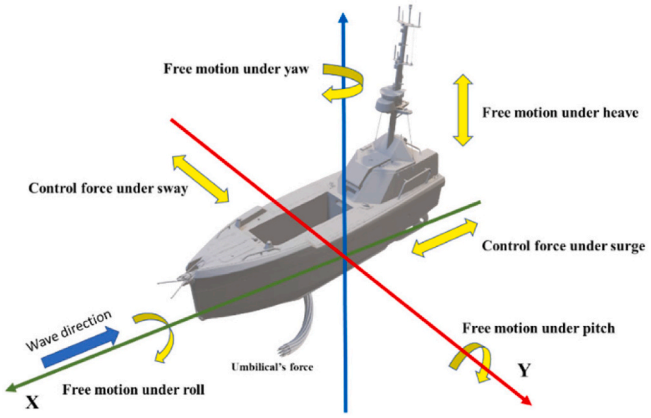

Fig. 2. The analytical model of the ASV: The control forces are applied in sway and surge directions.

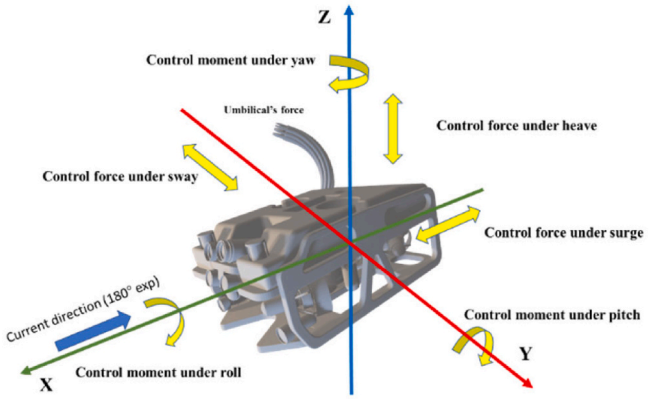

Fig. 3. The analytical model of ROV: The control forces and moments are applied under all 6 DOFs.

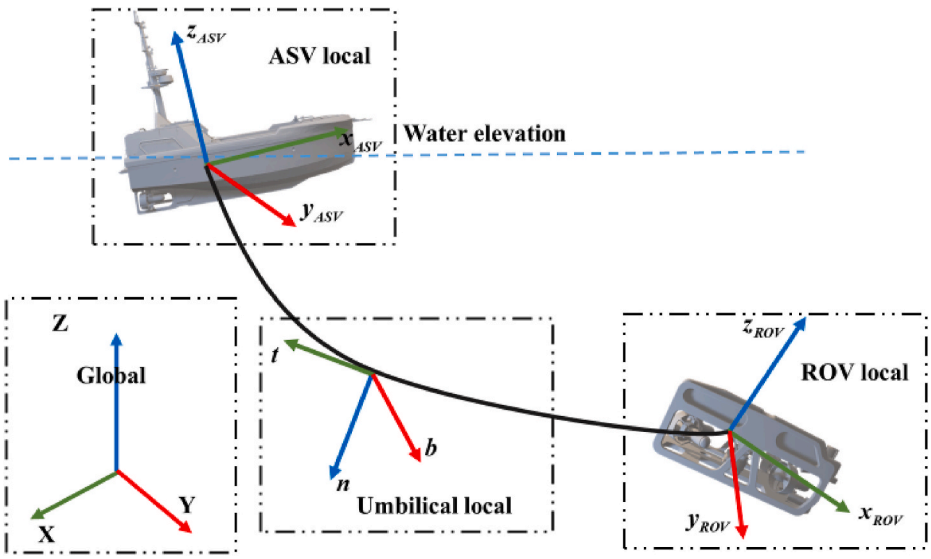

Fig. 1. The four coordinate systems of the ASV/ROV system.

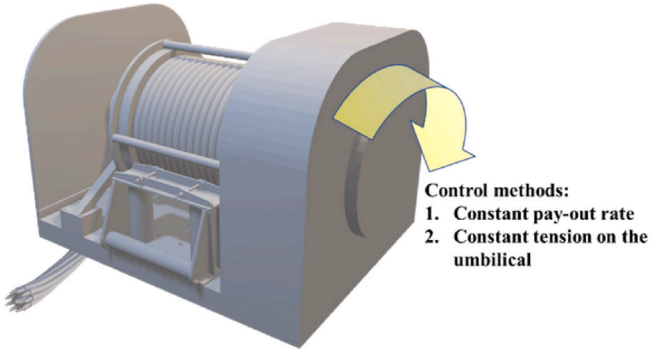

Fig. 4. The analytical winch model with two distinct control methods.

2. Analytical modelling of the ASV/ROV coupled system

2.1. Coordinate systems

The ASV/ROV coupled system is represented in four coordinates systems: i) the global coordinate, ii) the local coordinates of the ASV iii) local coordinates of the ROV and iv) the local coordinate along the umbilical (Fig. 1). The relationship between the global coordinates and the ASV/ROV local coordinates is described in terms of Euler angles (Fossen, 1999).

For the ROV,

$$[\mathbf{x_{ROV}} \quad \mathbf{y_{ROV}} \quad \mathbf{z_{ROV}}] = [\mathbf{X} \quad \mathbf{Y} \quad \mathbf{Z}] R_{ROV}(\theta_{ROV} \quad \phi_{ROV} \quad \gamma_{ROV}) \tag{1}$$

with

$$R_{ROV}(\theta_{ROV} \quad \phi_{ROV} \quad \gamma_{ROV}) = \begin{bmatrix} \cos\phi_{ROV}\cos\gamma_{ROV} & -\cos\theta_{ROV}\sin\gamma_{ROV} + \sin\theta_{ROV}\sin\phi_{ROV}\cos\gamma_{ROV} & \sin\theta_{ROV}\sin\gamma_{ROV} + \cos\theta_{ROV}\sin\phi_{ROV}\cos\gamma_{ROV} \\ \cos\phi_{ROV}\cos\gamma_{ROV} & \cos\theta_{ROV}\sin\gamma_{ROV} + \sin\theta_{ROV}\sin\phi_{ROV}\cos\gamma_{ROV} & -\sin\theta_{ROV}\sin\gamma_{ROV} + \cos\theta_{ROV}\sin\phi_{ROV}\cos\gamma_{ROV} \\ -\sin\phi_{ROV} & \sin\theta_{ROV}\cos\phi_{ROV} & \cos\theta_{ROV}\cos\phi_{ROV} \end{bmatrix}$$

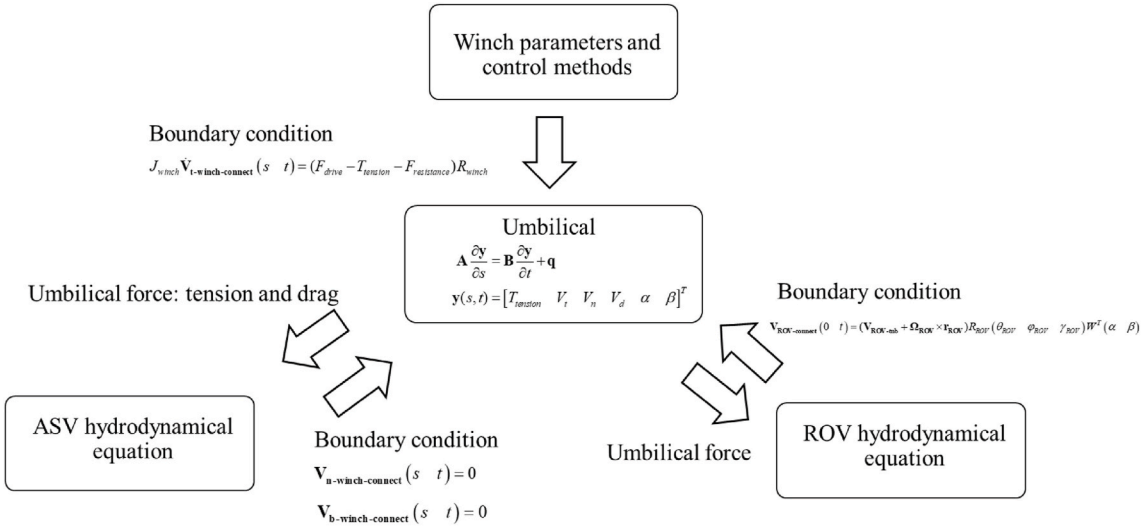

Fig. 5. Workflow of the coupled model.

Fig. 6. The modelled Autonomous Surface Vessel, CW7.

Table 2
The properties of the CW7.

Property	Value (unit)
Length	7.2 m
Beam	2.3 m
Draft	0.9 m
Weight (without payload)	4280 kg

Table 3
Properties of the modelled ROV.

Property	Value (unit)
Length	1 m
width	0.6 m
Height	0.5 m
Weight in the air (with the max payload)	74 kg
Weight in the water	5 kg
Max thrust	Forward $= 50\ kgf$
	Lateral $= 28\ kgf$
	Vertical $= 13\ kgf$

Similarly, the local coordinate ASV is,

$$[\mathbf{x_{ASV}} \quad \mathbf{y_{ASV}} \quad \mathbf{z_{ASV}}] = [\mathbf{X} \quad \mathbf{Y} \quad \mathbf{Z}] R_{ASV}(\theta_{ASV} \quad \phi_{ASV} \quad \gamma_{ASV}) \tag{2}$$

with

$$R_{ASV}(\theta_{ASV} \quad \phi_{ASV} \quad \gamma_{ASV}) = \begin{bmatrix} \cos\phi_{ASV}\cos\gamma_{ASV} & -\cos\theta_{ASV}\sin\gamma_{ASV} + \sin\theta_{ASV}\sin\phi_{ASV}\cos\gamma_{ASV} & \sin\theta_{ASV}\sin\gamma_{ASV} + \cos\theta_{ASV}\sin\phi_{ASV}\cos\gamma_{ASV} \\ \cos\phi_{ASV}\cos\gamma_{ASV} & \cos\theta_{ASV}\sin\gamma_{ASV} + \sin\theta_{ROV}\sin\phi_{ROV}\cos\gamma_{ROV} & -\sin\theta_{ASV}\sin\gamma_{ASV} + \cos\theta_{ASV}\sin\phi_{ASV}\cos\gamma_{ASV} \\ -\sin\phi_{ASV} & \sin\theta_{ASV}\cos\phi_{ASV} & \cos\theta_{ASV}\cos\phi_{ASV} \end{bmatrix}$$

where θ, ϕ, γ are the pitch, roll, and yaw angles of ASV and ROV, respectively.

In the umbilical local coordinate, **t**is the tangent to the umbilical in the direction of paying in/out from the winch and **b**is on the $(\mathbf{X}, \mathbf{Y})$ plane. Following the transform method form (Feng and Allen, 2004) allows to convert the local coordinate to the global coordinate based on three rotations: (a) a counter-clockwise rotation through an angle αabout the **Z** axis to bring the **X**axis into the plane of **t**and**n**; (b) a counter-clockwise rotation about the new the **X** axis through $\frac{\pi}{2}$to bring the **Z** axis into coincidence with **b**; (c) a clockwise rotation about βthrough **b**to bring **X** and **Y**into coincidence with **t**and**n**.

Thus, the relationship between these two coordinates can be presented as:

$$[\mathbf{t} \quad \mathbf{n} \quad \mathbf{b}] = [\mathbf{X} \quad \mathbf{Y} \quad \mathbf{Z}] W(\alpha, \beta) \tag{3}$$

with

$$W(\alpha, \beta) = \begin{bmatrix} \cos\alpha\cos\beta & -\cos\partial\sin\beta & \sin\alpha \\ -\sin\alpha\cos\beta & \sin\alpha\sin\beta & \cos\alpha \\ -\sin\beta & -\cos\beta & 0 \end{bmatrix}$$

2.2. ASV

The analytical model of the ASV is illustrated in Fig. 2. Owing to the control forces and the umbilical force are nonlinear, the governing equations(Yu et al., 2016) are presented under the time-domain as follows:

$$[M + m_\infty]\ddot{\xi}(t) + \int_{-\infty}^{t} H(t-\tau)\dot{\xi}(\tau)d\tau + ([K] + [C])\xi(t) + [F_u(t)] = [F_e(t)] \tag{4}$$

where $[M + m_\infty]$ is the mass matrix under 6-DOFs (including the added mass matrix for $\omega \to \infty m_\infty$), $H(t)$ is the retardation function matrix which can be obtained from the convolution integrals of frequency-dependent damping matrix H_d presented by (Cummins, 1962; Greco et al., 2009),

Table 4
Properties of the umbilical and winch.

Property	Value (unit)
Diameter	0.17 *m*
Weight in air	350 *kg*/*km*
Weight in water	150 *kg*/*km*
Minimum dynamic bending diameter	350 *mm*
Breaking strength	18 *kN*
Max allow tension	3 *kN*
Winch drum diameter	0.5 m
Winch drum mass	50 kg

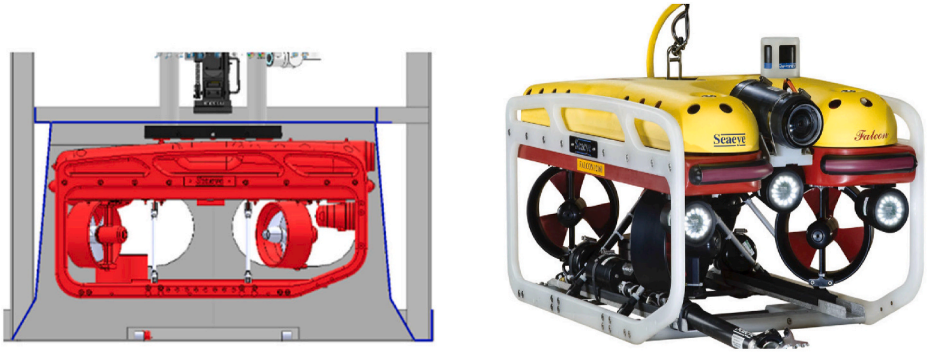

Fig. 7. Modelled ROV: (a) ROV Drawing with skid; (b) ROV as built.

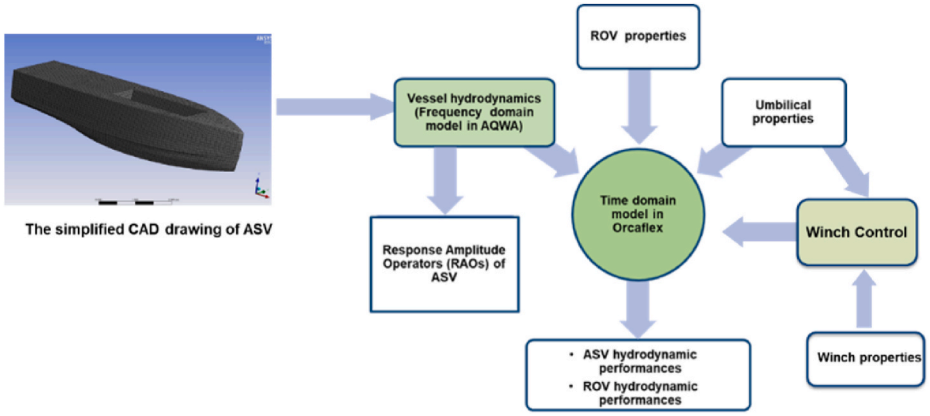

Fig. 8. Overview of the numerical model, including a frequency- and a time-domain model.

$[K]$ is the hydrostatic stiffness matrix, $[C]$ is the control force matrix, ξ is the ASV's motion equation, $[F_u]$ is the umbilical's force matrix and $[F_e]$ is the wave excitation force matrix. The hydrodynamic coefficients used in the Eq (4) have considered contributions and interactions from all 6-DOFs, which are calculated by a boundary solver AQWA.

The hydrostatic stiffness matrix has been added into the control force matrix and is written as:

$$[C] = \begin{bmatrix} C_1(x-x_0) & 0 & 0 & 0 & 0 & 0 \\ 0 & C_2(y-y_0) & 0 & 0 & 0 & 0 \\ 0 & 0 & 0 & 0 & 0 & 0 \\ 0 & 0 & 0 & 0 & 0 & 0 \\ 0 & 0 & 0 & 0 & 0 & 0 \\ 0 & 0 & 0 & 0 & 0 & 0 \end{bmatrix}$$

$$[K] = \begin{bmatrix} 0 & 0 & 0 & 0 & 0 & 0 \\ 0 & 0 & 0 & 0 & 0 & 0 \\ 0 & 0 & \rho g A_b & \rho g I_2 & -\rho g I_1 & 0 \\ 0 & 0 & \rho g I_2 & \rho g\left(I_{22}+I_3^V\right) - Mg(z-z_0) & -\rho g I_{12} & -\rho g I_1^V + Mg(x-x_0) \\ 0 & 0 & -\rho g I_1 & -\rho g I_{21} & \rho g\left(I_{11}+I_3^V\right) - Mg(z-z_0) & -\rho g I_2^V + Mg(y-y_0) \\ 0 & 0 & 0 & 0 & 0 & 0 \end{bmatrix}$$

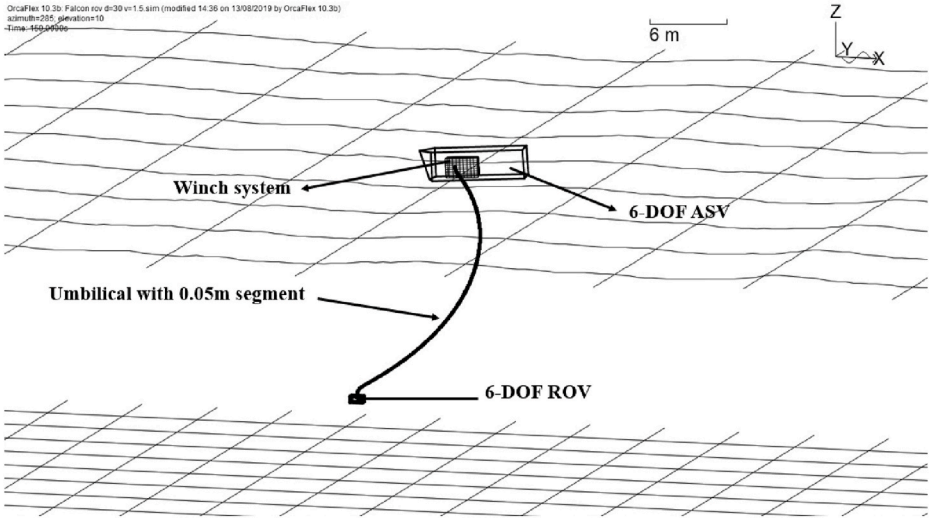

Fig. 9. The time-domain model in Orcaflex.

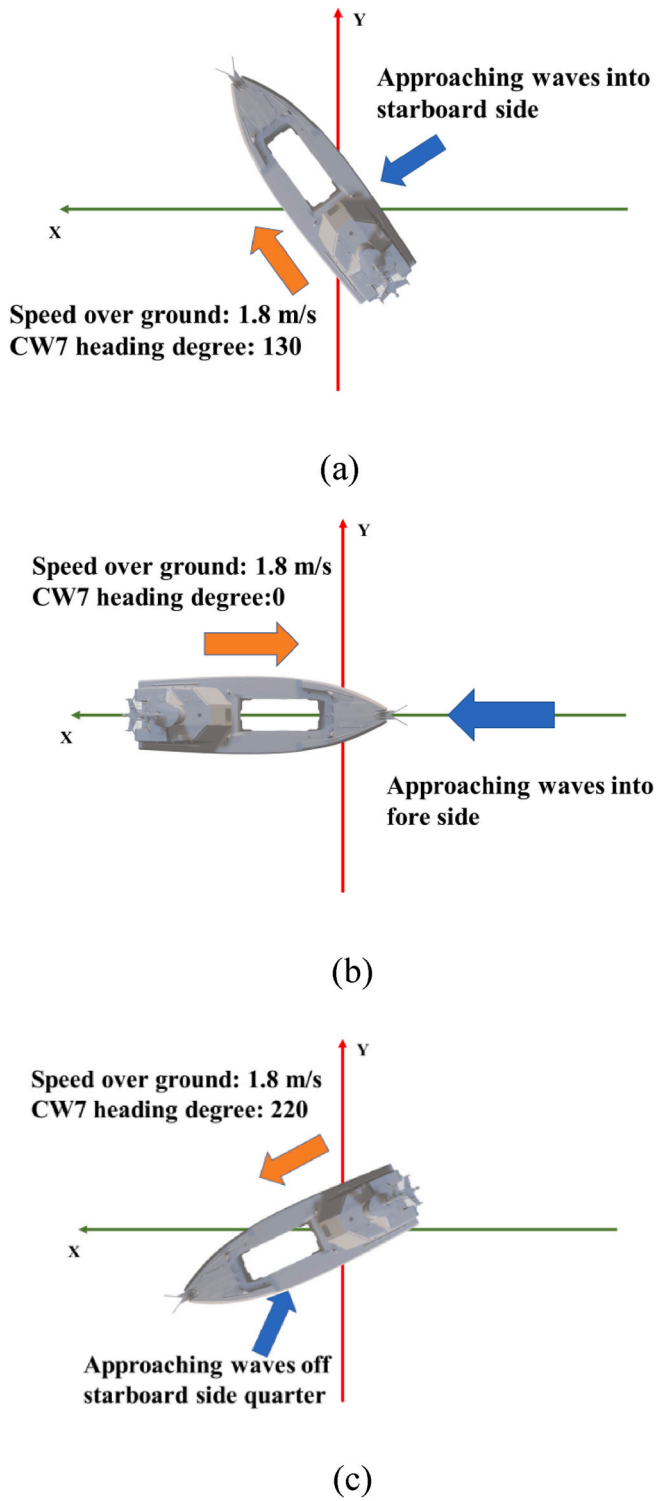

Fig. 10. Three situations are conducted during the sea trial: (a) Case a: Approaching wave into starboard side, heading degree, 130, velocity, 1.8 m/s; (b) Case b: Approaching wave into foreside, heading degree, 0, velocity, 1.8 m/s; (c) Case c: Approaching wave off the starboard side, heading degree, 220, velocity, 1.8 m/s.

where ρ is the water density, A_b is the heave area of the ship, I_i is the rotational inertia under the i^{th} degree of freedom (DOF), I_{ij} is the inertia under the i^{th} DOF due to the j^{th} DOF, x, y, z are the displacements along the $[\mathbf{X}\quad \mathbf{Y}\quad \mathbf{Z}]$ direction, z_0 is the static draft of the ship, x_0, y_0 are the desired holding positions under sway and surge, V is the ship's displaced volume. C_1, C_2 are the control force coefficients. During the time-domain calculation, if C_1, C_2 are large enough and the time step is sufficiently small, the ship will be limited at the desired location.

F_e is the sum of the Froude–Krylov force F_{FK} and the diffraction force F_d caused by the incident and diffracted waves, respectively (Falnes and Kurniawan, 2020).

$$F_{Ij} = -i\omega\rho \int_{S_{wet}} \phi_I\left(\vec{X}\right) n_j dS \tag{5}$$

$$F_{dj} = -i\omega\rho \int_{S_{wet}} \phi_d\left(\vec{X}\right) n_j dS \tag{6}$$

where ω is the wave frequency, ϕ_I is the incident wave potential, ϕ_d is the diffraction wave potential.

2.3. ROV

Fig. 3 presents the analytical model of the 6 DOFs ROV control forces and moments. As a result, the ROV in this paper is regarded as a 6 DOFs buoy. The associate mathematical model is presented in (Fang et al., 2007). The thrust control methods of ROV were presented in the (Zhao et al., 2020).

For the launch stage, the ROV is firstly driven with full thrusters so that it can quickly reach a depth to prevent it from colliding with the ASV. Then, the control method on the x, y direction offers a gentle way for the ROV's propeller force to increase as a function of its depth to the ASV:

$$F_{lx} = \left(x_{target} - x_{ROV}\right) * k_{lx} * log_2\left(z_{ASV} - z_{ROV}\right) \tag{7}$$

$$F_{ly} = \left(y_{target} - y_{ROV}\right) * k_{ly} * log_2\left(z_{ASV} - z_{ROV}\right) \tag{8}$$

When F_{lx} and F_{ly} are larger than the maximum thrust of ROV, the maximum thrusts will replace them.

The z-direction force F_{lz} includes a constant component C_z that permits to approach the target plus a Gaussian function around the target allowing the force to increase a lot when approaching the target in order to maintain the ROV's depth. Similar to the F_{lx} and F_{ly}, F_{lz} will still be limited by the maximum ROV thrust.

$$F_{lz} = C_z + k_{lz}\left(\frac{1}{5} e^{-\left(z_{ASV} - z_{ROV}\right)^2}\right) \tag{9}$$

where $x_{target}, y_{target}, z_{target}$ are the target coordinates in each direction; $x_{ASV}, y_{ASV}, z_{ASV}$ are the displacement of ASV in each direction; $x_{ROV}, y_{ROV}, z_{ROV}$ are the displacements of ROV in each direction; k_{lx}, k_{ly}, k_{lz} are the launch control coefficients in each direction.

During the holding or following stage, the control force is calculated as (here, the current direction is on the x-direction and heading to the ROV):

$$F_{following} = 0.5 * \pi * S_{Rd} * C_{ROV} * \left(-V_{cs} * 0.75 - V_{ASVX}\right)^2 \tag{10}$$

where S_{Rd} is the drag area of the ROV, C_{ROV} is the drag force coefficient on the x-direction, V_{cs} is the current speed on the surface, V_{ASVX} is the velocity of ASV in the x-direction. With this control force, the ROV can maintain the required distance to the ASV under the current and drag force load.

During the recovery stage, the control force is defined as a nonlinear relationship, which permits to be low when the ROV is far from the recovery target. It will become higher (limited by the maximum ROV thrust) when it approaches the target and low again when it reaches the target, without breaking the force continuity. The force is presented as follows:

$$F_{rx} = e^{-\frac{\left(x_{ASV} - x_{ROV}\right)^2}{10}} * k_{rx} * \left(x_{ASV} - x_{ROV}\right) \tag{11}$$

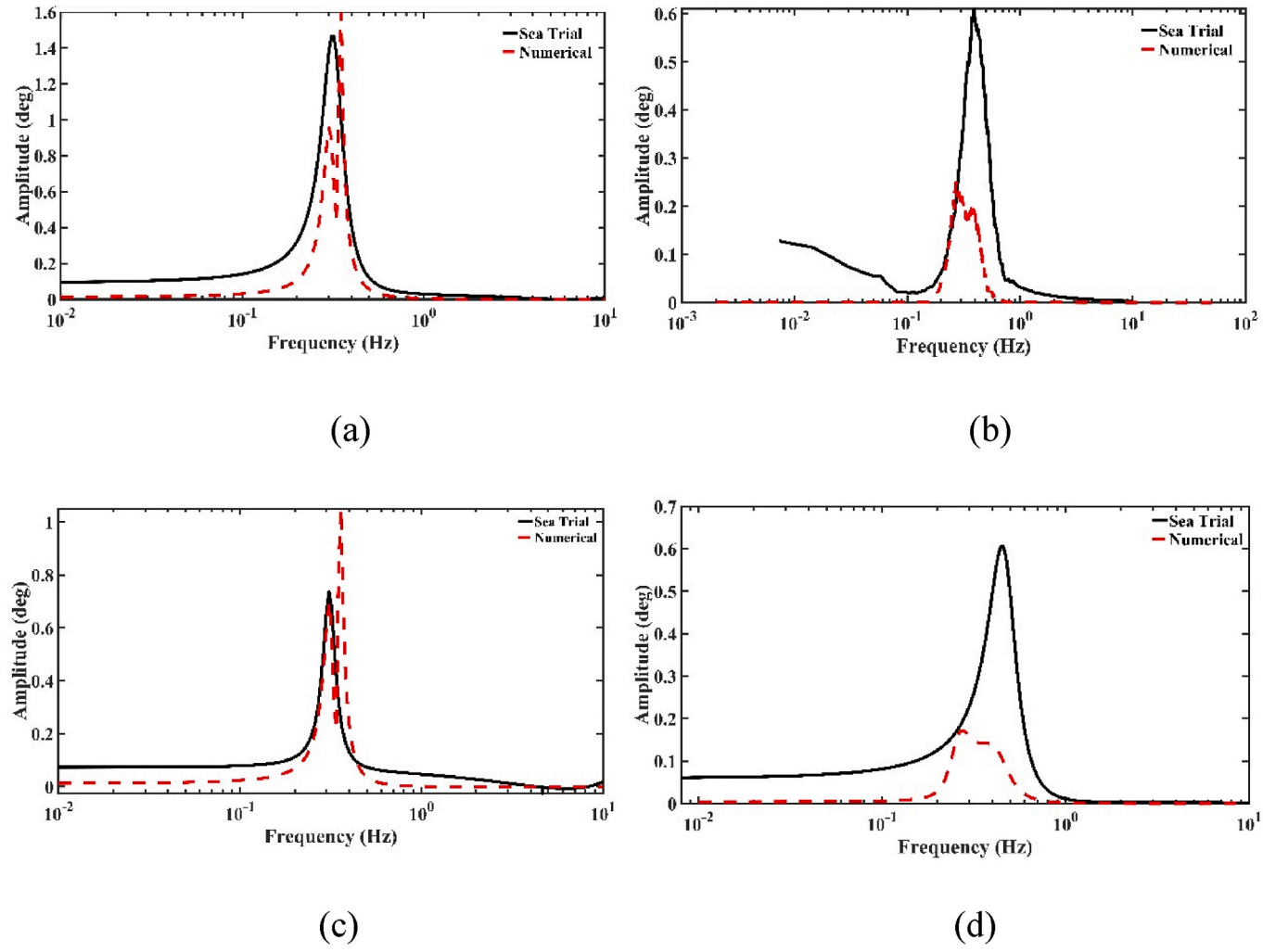

Fig. 11. The differences between results from sea trial and numerical simulations: (a) CW7 roll in the case a; (b) CW7 pitch in the case b; (c) CW7 roll in the case c; (d) CW7 pitch in the case c.

Table 5
The numerical cases layout.

No.	Target coordinate (x,y,z) (m)	The tidal current speed (water surface) (m/s)	Wave condition (JOWNSWAP)
1	(-10, 0, −30)	1	$H_s = 1.82m,\ T_p = 4s$
2	(-10, 0, −25)	1, 1.5, 1.75, 2	$H_s = 1.82m,\ T_p = 4s$
3	(-10, 0, −45)	1, 1.5, 1.75, 2	$H_s = 1.82m,\ T_p = 4s$
4	(-10, 0, −145)	1, 1.25, 1.5, 1.75	$H_s = 1.82m,\ T_p = 4s$

$$F_{ry} = (y_{ASV} - y_{ROV}) * k_{ry} \tag{12}$$

When the ROV is far from the ASV, $F_{rz} = 0$, however, if the ROV is in close proximity (here, the distance is less than 10 m) to the ASV, F_{rz} is half the maximum thrust of the propeller to keep the tension on the umbilical, preventing a sudden relative motion (and consequential snap loads) between ASV and ROV.where the k_{rx}, k_{ry} is the recovery control coefficients on the x- and y-directions. When the ROV is close enough to the ASV, the F_{rz} will be zero to prevent a collision.

2.4. Umbilical and winch

The umbilical and winch system couples the ASV and the ROV. Thus, the crucial task is to determine the umbilical dynamics. According to (Ablow and Schechter, 1983), umbilical dynamics can be generally expressed as:

$$\mathbf{A}\frac{\partial \mathbf{y}}{\partial s} = \mathbf{B}\frac{\partial \mathbf{y}}{\partial t} + \mathbf{q} \tag{13}$$

with

$$\mathbf{A} = \begin{bmatrix} 1 & 0 & 0 & 0 & 0 & 0 \\ 0 & 1 & 0 & 0 & V_b \cos\beta & -V_n \\ 0 & 0 & 1 & 0 & -V_b \sin\beta & V_t \\ 0 & 0 & 0 & 1 & V_n \sin\beta - V_t \cos\beta & 0 \\ 0 & 0 & 0 & 0 & -T_{tension} \cos\beta & 0 \\ 0 & 0 & 0 & 0 & 0 & T_{tension} \end{bmatrix}$$

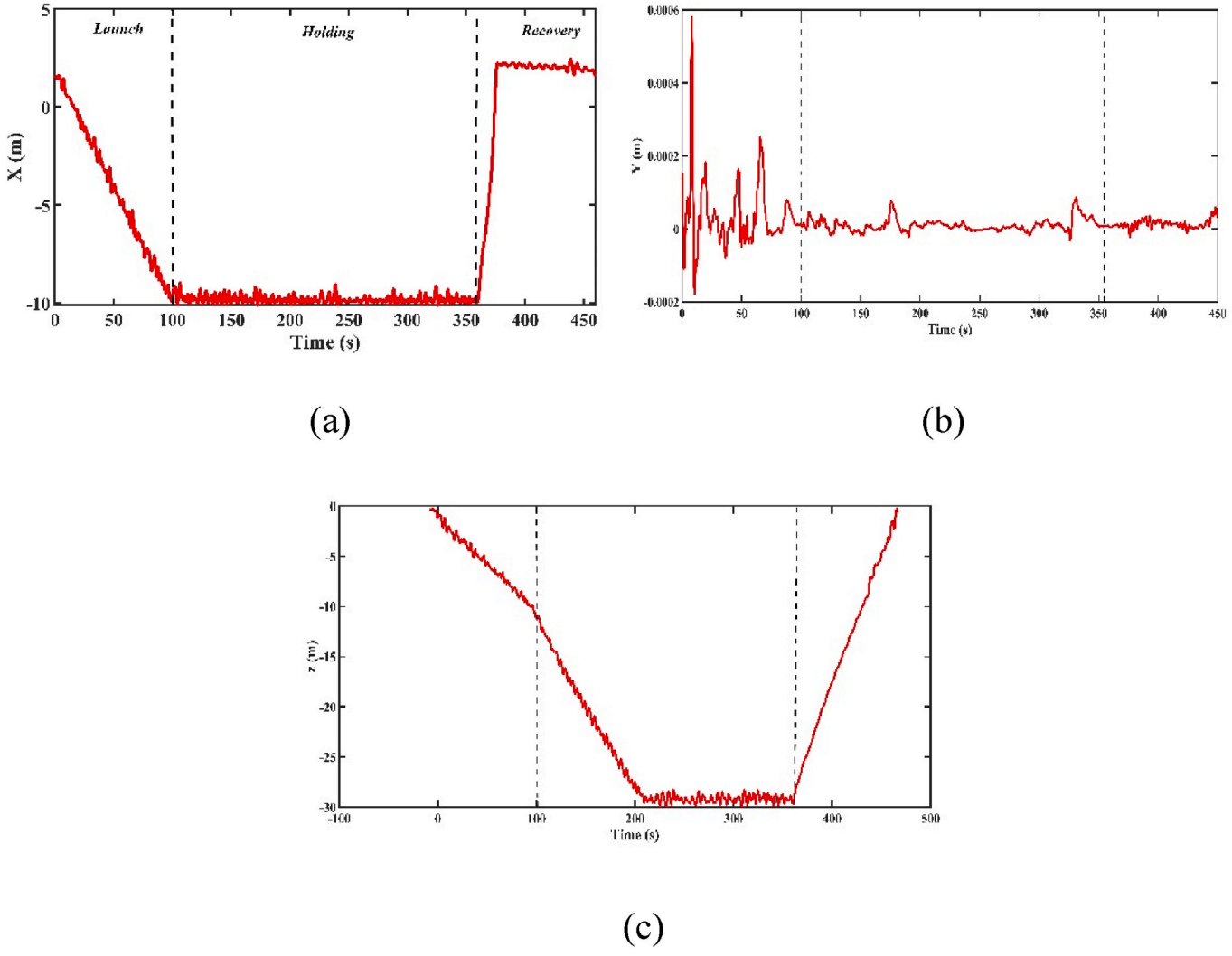

Fig. 12. The ROV position during the launch, holding, and recovery stage, the wave and tidal current are heading to the vessel: (a) x; (b) y; (c) z.

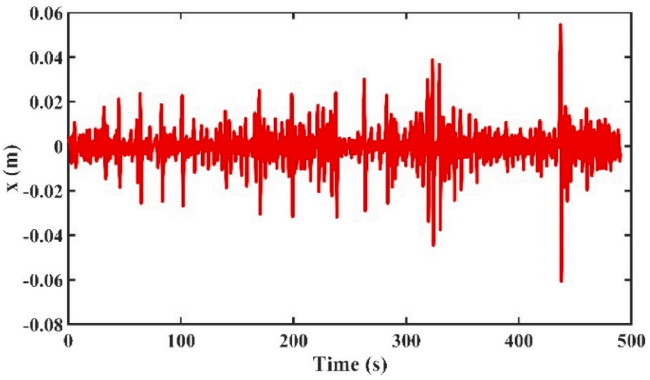

Fig. 13. *The ASV drift under.* $C_1 = 2000\ kN/m$

$$\mathbf{B}=\begin{bmatrix} -m_u e\dfrac{V_t}{1+eT_{tension}} & m_u & 0 & 0 & (m_{u1}V_b-\rho S_u J_b)\cos\beta & -(m_{u1}V_n-\rho S_u J_n) \\ e & 0 & 0 & 0 & 0 & 0 \\ 0 & 0 & 0 & 0 & 0 & 1+eT_{tension} \\ 0 & 0 & 0 & 0 & (1+eT_{tension})\cos\beta & 0 \\ -e\dfrac{m_{u1}V_b-\rho S_u J_b}{1+eT_{tension}} & 0 & 0 & m_{u1} & (m_{u1}V_n-\rho S_u J_n)\sin\beta-m_u V_t\cos\beta & 0 \\ -e\dfrac{m_{u1}V_n-\rho S_u J_n}{1+eT_{tension}} & 0 & m_{u1} & 0 & -(m_{u1}V_b-\rho S_u J_b)\sin\beta & m_u V_t \end{bmatrix}$$

$$\mathbf{q}=\begin{bmatrix} w_u\sin\beta+\dfrac{1}{2}\rho d\sqrt{1+eT_{tension}}\pi C_t U_t|U_t| \\ 0 \\ 0 \\ 0 \\ \dfrac{1}{2}\rho d\sqrt{1+eT_{tension}}C_n U_b\sqrt{U_b^2+U_n^2}-\rho S_u\dot{J}_b \\ w_u\cos\beta+\dfrac{1}{2}\rho d\sqrt{1+eT_{tension}}C_n U_n\sqrt{U_b^2+U_n^2}-\rho S_u\dot{J}_n \end{bmatrix}$$

where $\mathbf{y}$ is the dynamic vector of the umbilical, $\mathbf{y}(s,\ t)=[\ T_{tension}\quad V_t\quad V_n\quad V_d\quad \alpha\quad \beta]^T$; s is the arc length of the cable between the ASV and ROV; t is the time; $\mathbf{V_u}=[V_t\quad V_n\quad V_d]^T$ is the umbilical velocity matrix in its local coordinate; $T_{tension}=K_u\Delta l$, K_u is the spring coefficient, Δl is the deformation of the umbilical; m_u is the mass per unit length of umbilical; S_u is the cross-sectional area of the unstretched umbilical; e is the $1/ES_u$, E is the Young's modulus; m_{u1} denotes $m_u+\rho S_u$; The tidal current speed matrix in the umbilical coordinate is $\mathbf{J_u}=[J_t\quad J_n\quad J_d]^T$, and the relative speed between umbilical and current can be written as $\mathbf{V_u}-\mathbf{J_u}=[U_t\quad U_n\quad U_d]^T$; w_u is the $(m_u-\rho S_u)g$, g is the gravity acceleration.

To obtain the solution of equation(13), six boundary conditions will be needed. The two ends of the umbilical share the pay-out/in speed and the ROV speed, respectively. Thus, three boundary conditions are obtained.

For the ROV connection point, the ROV speed/angular speed on the $[\mathbf{t}\quad \mathbf{n}\quad \mathbf{b}]$ can be denoted as

$$\mathbf{V_{ROV-tnb}}=[V_{ROV-t}\quad V_{ROV-n}\quad V_{ROV-b}]^T \tag{14}$$

$$\Omega_{\mathbf{ROV}}=[u_{ROV-pitch}\quad v_{ROV-roll}\quad w_{ROV-yaw}]^T \tag{15}$$

According to the (1) and (3), the relationship between ROV and umbilical coordinate could be expressed as:

$$[\mathbf{t}\quad \mathbf{n}\quad \mathbf{b}]=[\mathbf{x_{ROV}}\quad \mathbf{y_{ROV}}\quad \mathbf{z_{ROV}}]R_{ROV}^T(\theta_{ROV}\quad \phi_{ROV}\quad \gamma_{ROV})W(\alpha,\beta) \tag{16}$$

In terms of (14) - (16), the boundary conditions (three boundaries) of ROV connected point could be obtained.

$$\mathbf{V_{ROV-connect}}(0,t)=(\mathbf{V_{ROV-tnb}}+\mathbf{\Omega_{ROV}}\times\mathbf{r_{ROV}})R_{ROV}(\theta_{ROV}\quad \phi_{ROV}\quad \gamma_{ROV})W(\alpha,\beta) \tag{17}$$

Here, the length of umbilical at this point is considered as 0, $\mathbf{r_{ROV}}$ is the distance between the mass centre and the connecting point on the ROV.

At the winch connected point, the umbilical speed at $\mathbf{b},\mathbf{n}$direction is zero:

$$\mathbf{V_{n-winch-connect}}(s,t)=0 \tag{18}$$

$$\mathbf{V_{b-winch-connect}}(s,t)=0 \tag{19}$$

The last boundary condition is obtained through the dynamic equation of the winch based on Newton's Law:

$$J_{winch}\dot{\mathbf{V}}_{\mathbf{t-winch-connect}}(s,t)=(F_{drive}-T_{tension}-F_{resistance})R_{winch} \tag{20}$$

where J_{winch} is the moment of inertia of the drum, $F_{resistance}$ is the resistance of the drum, R_{winch} is the radius of the drum.

The six boundary conditions [(16) to (20)] can be used to solve the equation (13). In the real sea environment, the $\mathbf{V_{t-winch-connect}}(s,t)$ is always non-zero and dependent on the winch control method. The boundaries and solutions with a non-zero $\mathbf{V_{t-winch-connect}}(s,t)$ are described in (Feng and Allen, 2004).

In this present paper, two different methods are used (see also Fig. 4).

1. The first method, *pay-out control*, is to maintain the pay-out rate (v_{out}) of the umbilical as a constant value, and then to calculate the winch drive force (F_{drive}) in the umbilical at any time.
2. The second method, tension *control*, aims to control the tension and to determine the corresponding pay-out rate, respectively.

For the pay-out control,

$$\mathbf{V_{t-winch-connect}}(s,t)=v_{out} \tag{21}$$

As a result, the $\dot{\mathbf{V}}_{\mathbf{t-winch-connect}}(s,t)$ is 0.

The winch drive force is:

$$F_{drive}=T_{tension}+F_{resistance} \tag{22}$$

The resistance of the winch could be presented as:

$$F_{resistance}=d_{db}+c_{out}v_{out}+d_{out}{v_{out}}^2 \tag{23}$$

where d_{db} is the winch drive dead-band, c_{out} are the winch drive damping terms for pay-out. d_{out} are the winch drive drag terms for pay-out.

For the tension control method:

$$F_{drive}=F_{target}+F_{resistance} \tag{24}$$

where F_{target} is the target tension on the umbilical.

According to equations (6)–(8) and $J_{winch}=M_{winch}R_{winch}^2$

$$v_{out}(s,t)=\frac{(F_{target}-T_{tension})}{M_{winch}R_{winch}}t+v_{out}(s_0,0) \tag{25}$$

When the solutions of equation (13) are obtained, the umbilical force, including tension and drag force, can be converted into the global coordinates and used to solve the ASV and ROV hydrodynamic issues. The overall workflow of this coupled model is illustrated in Fig. 5.

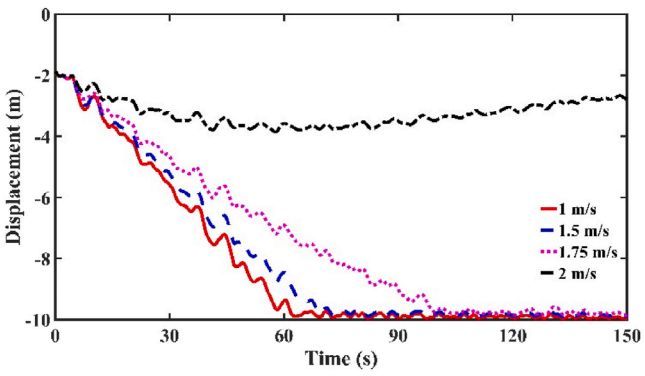

(a)

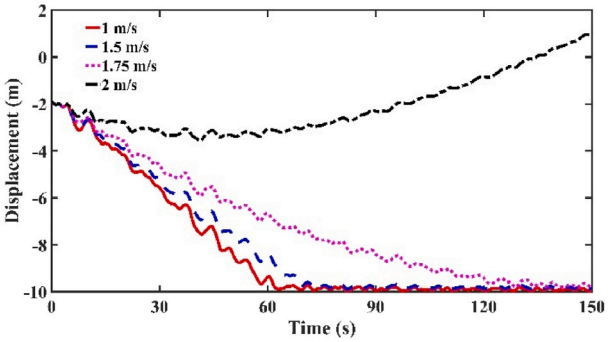

(b)

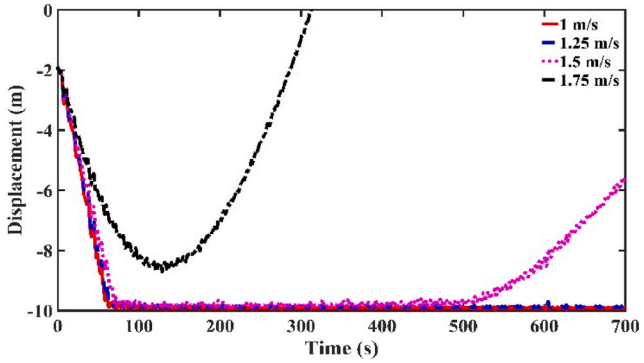

(c)

Fig. 14. The tidal current capacity of the Falcon ROV, the current direction is heading towards the ROV: (a) Water depth is 30m, target depth is 25m; (b) Water depth is 50m, target depth is 45m; (c) Water depth is 150m, target depth is 145m.

3. Case study

3.1. System description

For this case study, two specific sub-systems have been selected, the L3 Harris ASV CW7 (L3HARRIS, 2020) and the Falcon ROV (SEAEYE, 2020). The two are coupled through a winch system, installed on the ASV. The details of this system are illustrated in the following section.

3.1.1. ASV sub-system

CW7 is a multi-role work class ASV, which is suitable for offshore tasks, such as subsea positioning, surveying and environmental monitoring. C.W. 7 integrates a variety of payloads including multibeam, ultra-short baseline (USBL), sondes and acoustic Doppler current profilers (ADCP) via exchangeable payload frames. The details of CW7 can be seen in Fig. 6 and Table 2.

3.1.2. ROV

The modelled ROV is pictured in Fig. 7, and properties are summarised in Table 3 Properties of the modelled ROV. The ROV is propelled by four vectored thrusters, with maximum thrusts of forward = 50 kgf, lateral = 28 kgf and vertical = 13 kgf.

3.1.3. Winch and Umbilical

The properties of the winch system that is designed to be installed on the ASV and the umbilical are summarised in Table 4, which lists the physical characteristics of umbilical that is used in the winch system.

3.1.4. Model illustration

An overview of the modelling scope is provided in Fig. 8. The numerical simulation includes a frequency- and a time-domain model. The hydrodynamic forces of the ASV, are calculated as the sum of diffraction (including excitation and Froude-Krylov forces) and radiation forces, obtained by AQWA a frequency-domain boundary element method solver. The simplified CAD drawing used as an input for AQWA to calculate the Response Amplitude Operators (RAOs) is also shown in Fig. 8. The physical properties of ROVs and umbilical configurations are implemented in a fully coupled nonlinear hydrodynamic time-domain model (Orcaflex) to estimate the response, forces and loads experienced by the vessel, ROV and the umbilical cable, shown in Fig. 9.

3.1.5. Validation

This paper draws on data from numerical and operational measurements from field deployments (cases are illustrated in Fig. 10). The environment of the sea trial is not exactly measured but is defined by a JONSWAP spectrum with a significant wave height H_s = 0.3 m, peak wave period T_p is 3s, based on the location of the sea trial. A motion sensor installed on the CW7 prototype captured the hydrodynamic response in pitch and roll. Results from both sea trial and numerical model have been converted into the frequency-domain via Fourier transform, allowing a direct comparison. Fig. 11 presents the dominant motions for each case (roll for case a, pitch for case b, and roll and pitch for case c). For all cases, the spectrum bands of sea trial and simulations are in acceptable agreement while the band for the sea trial is slightly wider. This may be caused by the 2nd-order wave drifting during the sea trial, which is challenging to replicate in the numerical simulations exactly. However, differences in the amplitude are more significant. The effects caused by liquid viscosity can potentially influence the roll amplitude. This effect will result in an apparent lower peak roll amplitude during the sea trial [Fig. 11 (a) and (c)]. The pitch response is less sensitive to the viscosity [Fig. 11 (b) and (d)], a higher peak is observed in the sea trial, which may be caused by different incident waves in the sea trial compared to simulations. The irregular wave used in the numerical model is similar, but due to the stochasticity not identical to the sea trial conditions. Ideally the ASV/ROV system should be validated. Our current sea trial data only include the ASV roll and pitch motion, as a result, a stricter validation based on the basin test will be conducted in further research.

4. Results

The numerical cases (Table 5) include a range of targets and environment conditions for the given ASV/ROV to explore i) the ROV performance in different tidal current and target scenarios, ii) the stability of the ASV, iii) umbilical tension and iv) the required winch power. In all

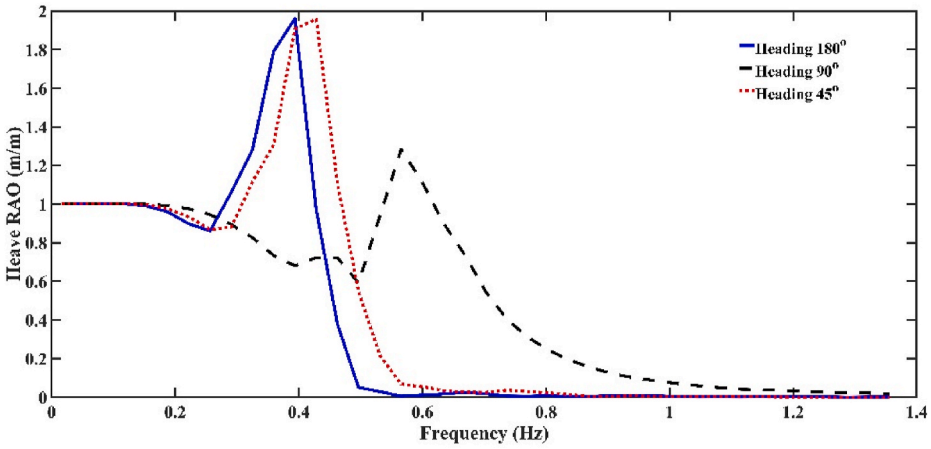

(a)

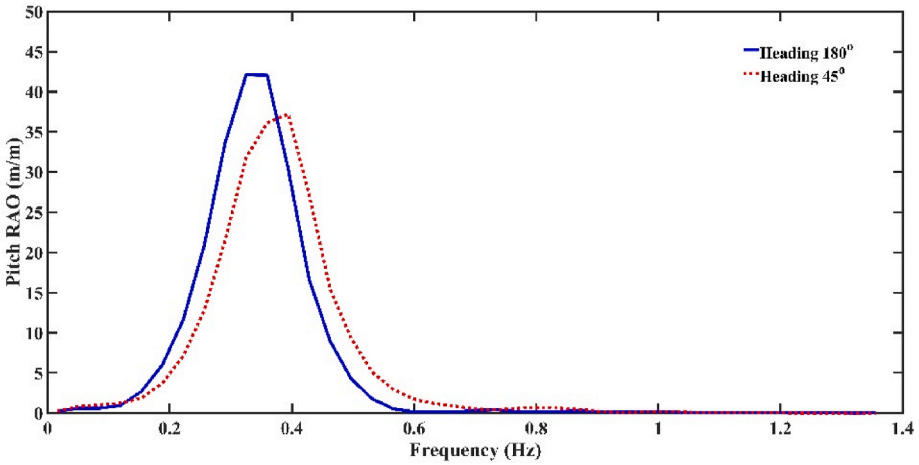

(b)

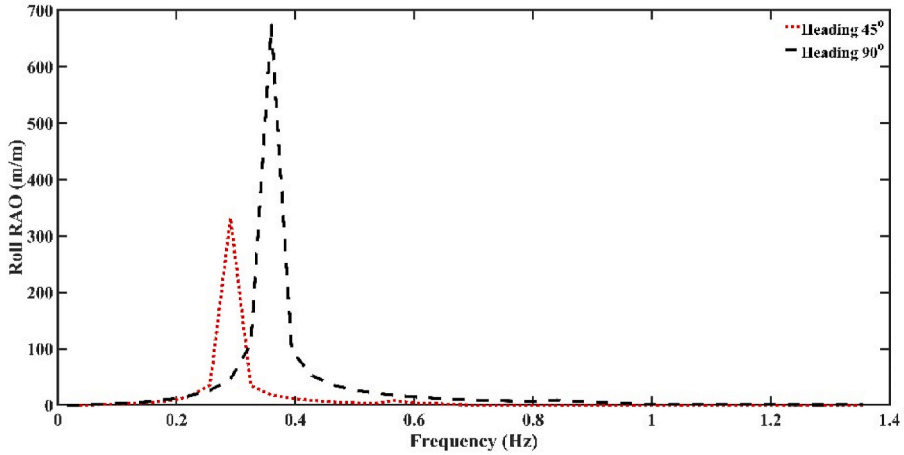

(c)

Fig. 15. CW7 heave, pitch, and roll RAOs for three incident wave directions: (a) Heave RAO, Peak amplitude with heading 180° is 1.98 with 0.4Hz. Peak amplitude with heading 45° is 1.96 with 0.43 Hz. Peak amplitude with heading 90° is 1.3 with 0. 6Hz;(b) Pith RAO, Peak amplitude with heading 180° is 43 with 0.38Hz. Peak amplitude with heading 45° is 36 with 0.42 Hz; (c) Roll RAO, Peak amplitude with heading 45° is 310 with 0.26Hz. Peak amplitude with heading 90° is 690 with 0.39 Hz.

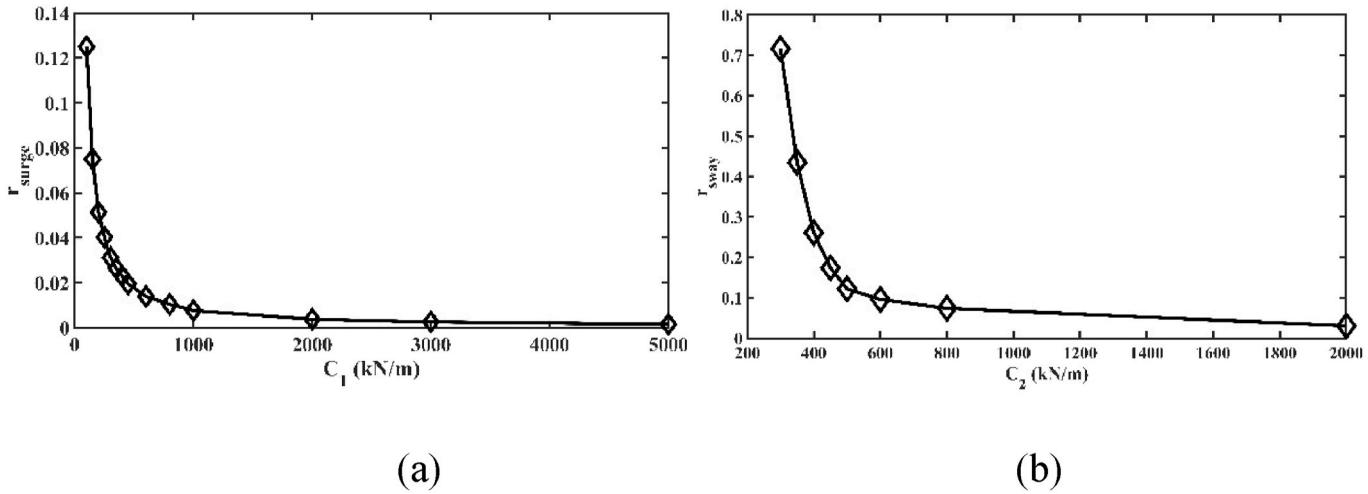

Fig. 16. Normalised drifting of the CW7: (a) Surge; (b) Sway.

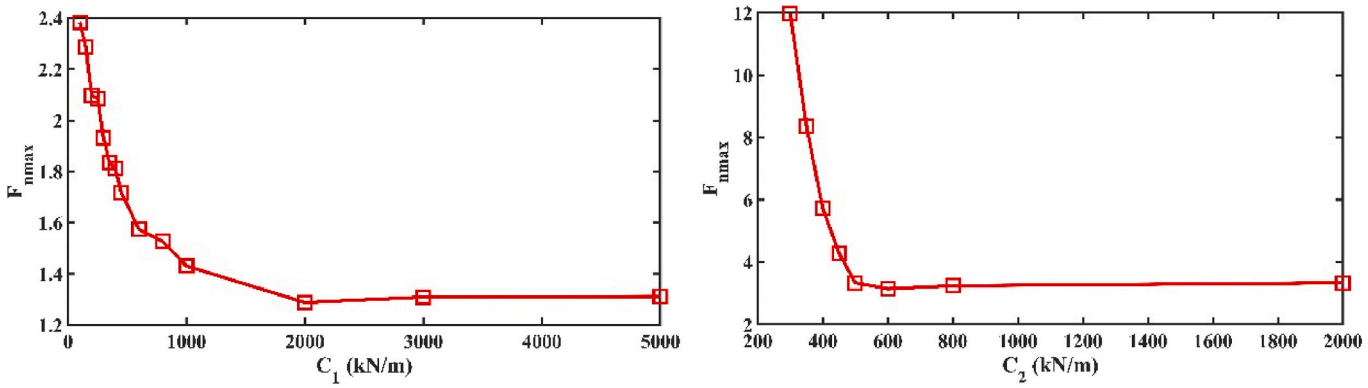

Fig. 17. Normalised maximum control force: (a) Surge: (b) Sway.

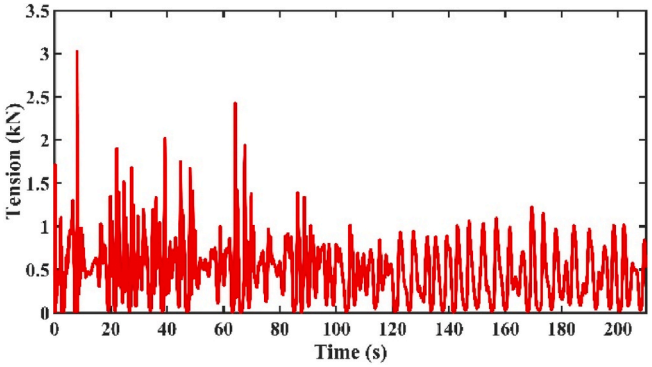

Fig. 18. *The umbilical tension during the launch stage: the relatively higher tensions appear when the.t* $< 100\,s$

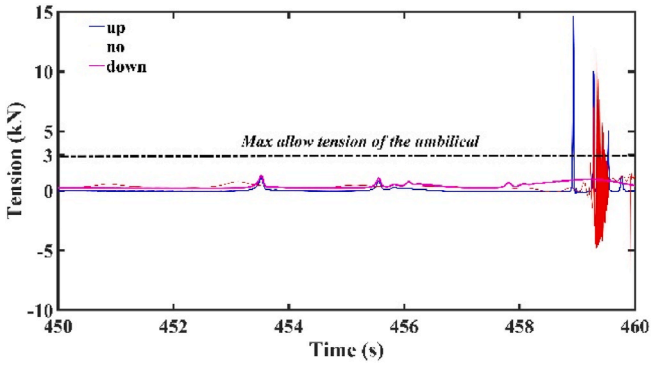

Fig. 19. The umbilical tension when the Falcon is close to the CW7: The Falcon reaches the water surface at 460 s.

cases, the approaching waves and currents have the identical direction which is heading to the ASV.where H_s is the significant wave height, $T_p$is the peak wave period.

Fig. 12 presents the ROV position coordinates to reach a target location of z-coordinate: 30 m, x-coordinate: 10 m, and y-coordinate: 0 m. To reduce computational intensity of the model, the incident wave and currents original are heading (parallel) to the ASV. Besides, the y coordinate of ROV target in the Fig. 12 is zero which means the umbilical tension on the y-direction is almost 0, too. As a result, the drift is almost 0. The time-series include launch, holding and recovery stages. The ASV's drifting motions are shown in Fig. 13.

4.1. Tidal current capacity of FALCON

Tidal capacity, i.e. what is the threshold tidal current the ROV is able to overcome to reach its target, is the critical parameter for the ROV design, particular for the launch stage. The tidal capacity of Falcon launch stage is explored with 30 m, 50 m, and 150 m water depth. The x- and y-coordinates of target positions are identical (10 m, 0 m) while the z-coordinates are 25 m, 45 m, and 145 m for each water depth. The tidal

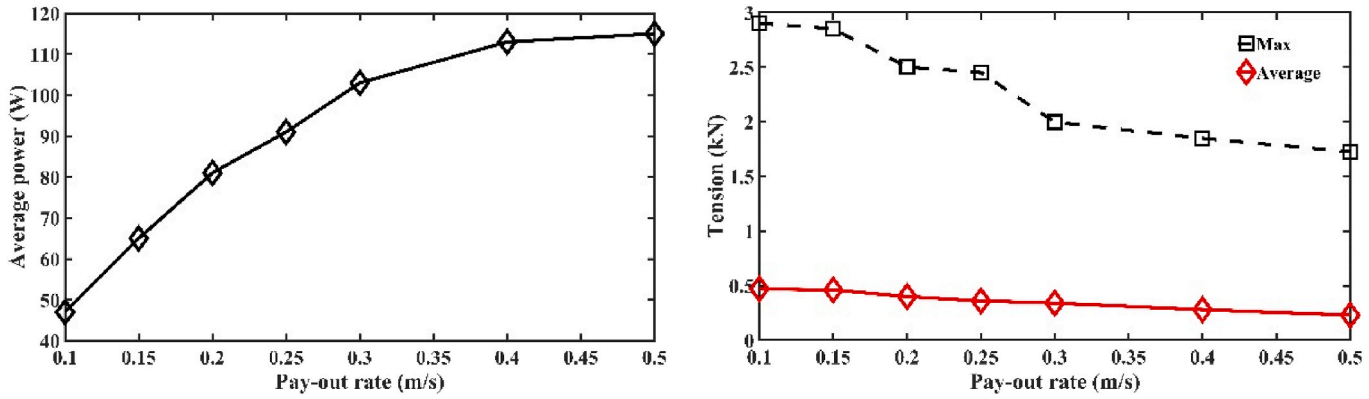

Fig. 20. Winch performance for the pay-out rate control method: (a) Average winch power; (b) Umbilical tension.

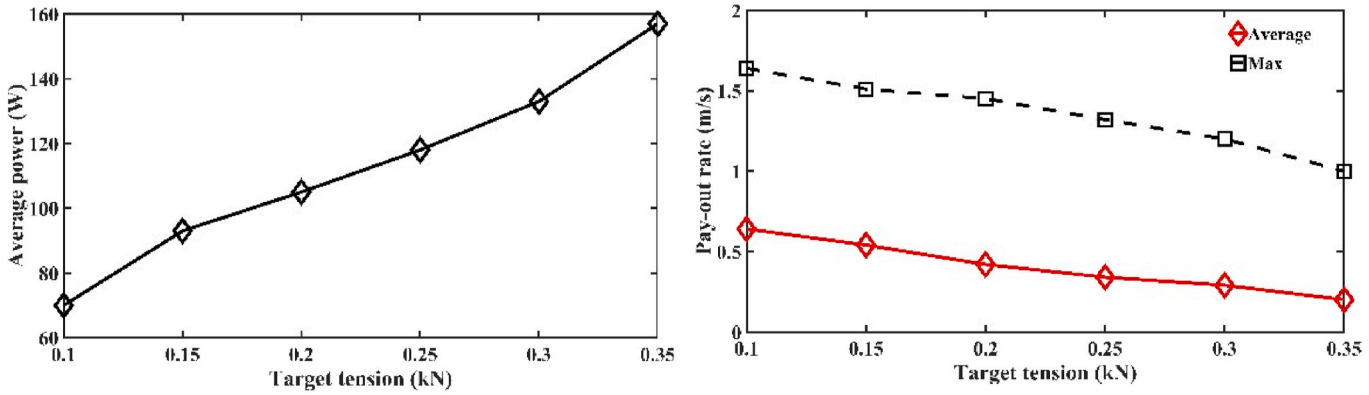

Fig. 21. Winch performance for tension control method: (a) Average winch power; (b) Umbilical tension.

current is defined by the power-law method, and its direction is fixed and does not vary with depth. The current speed S_c varies with the water depth.

$$S_c = S_b + \left[(S_f - S_b) \frac{z - z_b}{z_f - z_b} \right]^{1/p} \tag{26}$$

where S_f and S_b are the current speeds at the surface and the seabed, respectively; p is the power law exponent; z_f is the z-coordinate of the still water level; z_b is the z-coordinate of the seabed.

The Falcon tidal current capacity is shown in Fig. 14. The current heading to the Falcon is regarded as an extreme situation. The results determine that the current capacity is 1.75 m/s during 30 m and 50 m water depth and this capacity will reduce to 1.5 m/s when the water depth is 70m and 1.25 m/s with 150 m water depth.

4.2. Stabilities of CW7

4.2.1. Response amplitude operator

The stability of CW7 in the frequency-domain is discussed in terms of its motion RAO (Bonaschi et al., 2012).

Fig. 15 shows the RAOs of CW7 for different wave directions, which are identical to that in the sea trial, while the velocity of the vessel is set to be zero. It can be observed that differences in the peak heave RAO between heading 180° and heading 45° are small (0.39 Hz and 0.42 Hz). When the approaching wave direction is 90°, the heave RAO has the largest discrepancy and offset. The wave direction also influences the frequency of the peak heave RAO. It can be determined that the frequency relating the peak RAO is higher under a larger intersection angle between vessel and incident wave. The rotation RAO (pitch or roll RAO) is quite small for cases with heading 180° or heading 90° (the peak pitch RAO with heading 90° and roll RAO with heading 180° are all below one). Therefore, the rotation RAO is only discussed with two incident wave directions. Similar to the heave RAO, the wave approaching direction affects both the vessel peak amplitudes and peak frequency in pitch and roll cases.

4.2.2. Control coefficients

The CW7control forces are defined by the control coefficients C_1, C_2in Eq.(4) and the drifting distance from the target position. This section discusses C_1, C_2 under an extreme wave condition($H_s = 1.82m$, $T_p = 4s$), and the drifting distance is normalised by the CW7 length and beam, respectively. Fig. 16 exhibits the normalised drifting under surge and sway during cases with heading 180° and 90°.

$$r_{surge} = \frac{0.5*(D_{surge-p} + D_{surge-n})}{vessel\ length} \tag{27}$$

$$r_{sway} = \frac{0.5*(D_{sway-p} + D_{sway-n})}{vessel\ beam} \tag{28}$$

It is shown that when the control coefficient exceeds a specified value (here, 1000 kN/m for surge and 800 kN/m for sway), vessel drifting will be very small and steadily decreasing towards 0.

The normalised maximum control force (F_{nmax}) is illustrated in Fig. 17.

$$F_{nmax} = \frac{F_{\max}}{vesselweight} \tag{29}$$

The changing trend of $F_{nmax}$is similar to the surge and sway drifting. When the coefficient is relatively small, the F_{nmax} will be very large.

4.3. Umbilical and winch

4.3.1. Umbilical tension

The wave condition is identical to that in section 4.2.2 ($H_s = 1.82m$, $T_p = 4s$). with a 1 m/s tidal current. Fig. 18 and Fig. 19 present the tension on the umbilical during the launch and recovery stages, respectively.

4.3.2. Winch power

The winch control strategy employs two control methods, based on i) maintaining the pay-out rate and ii) maintaining the tension of the umbilical. The average winch power is calculated by: $\overline{P_{winch}} = \frac{\int_0^T F_{tension}(t)v_{out}(t)dt}{T}$.

Fig. 20 shows the winch performance with a pay-out rate control method. $\overline{P_{winch}}$ increases and converges towards a constant value for higher pay-out rates, while the umbilical tension decreases, significantly. If the pay-out rate is close to the diving rate of the ROV, the interaction force between the umbilical and the ROV will be reduced, leading to both smaller maximum and smaller average tension (see Fig. 20 (b)). Considering the maximum allowable tension, 0.1 m/s pay-out rate seems to be the most suitable choice for this particular winch system.

The winch performance under tension control is presented in Fig. 21. Although the pay-out rate has an apparent decrease in increased target tension, the winch power still increases.

5. Discussion

This study used a time and frequency domain method to discuss the hydrodynamic performance of the ASV/ROV system. With the help of this model, several nonlinear factors such as coupled effects between the ASV and ROV, control strategies of the ROV and the winch system could be taken into consideration. Results presented in section 4 demonstrated that these nonlinear coupled factors had a considerable impact on the capability and performance of the ASV/ROV system.

For the whole ASV/ROV system, the results shown in Figs. 12 and 13 demonstrated the launch and recovery control strategy used in this study is feasible for the chosen system. The modelling approach is applicable to assess similar system design and capacity questions. When the ROV reaches the target position on the x-direction, the control method can maintain the position of ROV on the x-direction for different water depths. The fluctuation of the ROV position caused by the relative motion between the ASV and ROV always remains at a low level (less than 2% of target water depth) during the whole launch and recovery phase. The drifting of the ASV is not significant with a linear control force.

For the ROV, its tidal current capacity shows a strong dependency with regards to the target water depth. When the target depth of the ROV is larger, the ROV needs a longer umbilical. The drag force caused by the tidal current will be more significant, leading the current capacity of the ROV to decreases. This capacity modelling is important to determine the correct ROV for a specific site/mission/target depth for given environmental conditions.

Regarding the ASV, the frequency of the peak RAO depends on the incident wave directions. This is believed to be caused by the coupled added mass of the CW7 on the different DOFs (such as a_{12}, a_{13} , etc.) in the frequency model. Furthermore, the roll RAO of the CW7 exhibits the most significant amplitude. A possible explanation is that the model used in this study is based on the potential flow theory. Therefore, nonlinear effects caused by the liquid viscosity could not be considered without any basin tests results, and these effects are the most significant at the natural roll frequency.

The results of the ASV drifting behaviour show that the large control coefficients, effectively the vessel thrusts, can reduce both drifting distance and maximum amplitude of the control force (F_{nmax}). As described in section 2, the wave load on the CW7 is the sum of the radiation and excitation wave forces. The large coefficients will decrease the drifting velocity of the vessel, which can decrease the wave radiation force. In these cases, the control force mainly dominates the wave diffraction forces.

For the winch system, the maximum tension appears before $t = 100s$ for the sudden relative motion between ASV and ROV caused by the steep wave during the launch stage. The maximum tension is still smaller than the maximum allowable tension ($3kN$) during this period. If the time exceeds 100s, the umbilical is long enough to buffer these relative motions, maintaining the tension amplitude below $1.5kN$ (see Fig. 18). For the launch stage, the extreme tension also appears when the ROV is close to the ASV. In this strategy, a down-control force is used to reduce this extreme tension. Fig. 19 compares the tension during cases with non-, up-, and down-vertical control force. The results demonstrate that a down-control force is a feasible solution to limit the sudden peak tension. The maximum tension amplitude is less than half of max allowable tension ($3kN$). Cases with up- and no-control force both exceed the umbilical max allow tension ($3kN$) while still below the breaking tension. Slight negative tension, i.e. compression, can be observed in up- and no-forces cases, which should ideally be avoided to maintain umbilical integrity.

Comparing the two control methods of the winch, the tension control allows the ROV to reach the target location quicker, whilst only requiring slightly higher power. The umbilical tension in the tension control also can be limited to a relatively lower level to enhance the stability of the system. The tension control seems to be more feasible during the numerical simulation; however, other practical engineering factors such as the maximum pay-out rate and the overall system cost should be considered for the system engineering as well.

This coupled model and research methods presented in this study have provided some new insights into the ASV/ROV design and application. However, the range of applicability of the present model should also be stated explicitly here. The model is based on the potential flow theory. Thus, the additional hydrodynamic viscous damping of the ASV should be quantified through experimental decay tests in the future. Additionally, the ROV hydrodynamic coefficients will be changed by ASV, especially when the ROV is close to the ASV. This paper did not consider this change in current stage. A future experiment to quantify the exact coefficients is also required. The control method of the ROV should be optimised based on the different target position and environmental conditions. New control methods, e.g. based on machine learning could be tested and employed when sufficient data from sea trials, are obtained (Anderlini et al., 2018; Kim and Yu, 2016). Finally, more details of the winch such as the damping, the mechanical energy loss, and the dead band should be taken into consideration to refine the model.

6. Conclusions

This paper evaluated the hydrodynamic performances of an unmanned vessel system for an entire launch and recovery cycle. The hydrodynamic time-domain model of the ASV/ROV coupled system is described in detail, enabling similar design and engineering studies for coupled systems. In the presented model, different boundary conditions are used to solve the dynamics of the umbilical in order to get winch performance under different control methods. The results present a specific the case study, for a system including the ASV (CW7), ROV (Falcon), umbilical and winch. Results of the case study demonstrate the feasibility of the control strategy and system performance. Key findings include:

a) The tidal current capacity of the ROV shows significant dependency on its target depth. A lager target depth will lead to a smaller ROV current capacity. For the Falcon, its capacity is 1.75 m/s during 30 m and 50 m water depth, and it will reduce to 1.5 m/s when the water

depth is 70m. It reduces even further to 1.25 m/s for the 150 m water depth.

b) During the launch stage, the maximum umbilical tension caused by the steep approaching waves appears when the $T < 100\,s$. Once sufficient cable length is paid out, the loads are buffered/decoupled. For the recovery stage, the down-control force offers a feasible solution to reduce the peak tension caused by the sudden relative motion between ASV and ROV.

c) By comparing the pay-out rate and tension control methods, the tension control allows the ROV to reach the target faster with a slightly higher power.

These results demonstrate that the coupled effects between ASV and ROV significantly influence the whole system stability and capacity. Additionally, the winch exhibits the different tension range and power consumption under two control methods. The methods and finding of this study will be able to inform the engineering design and modelling of such coupled systems in order to progress towards autonomous launch and recovery operations.

CRediT authorship contribution statement

Chenyu Zhao: Conceptualization, Methodology, Software, Data curation, Writing – review & editing, Writing. **Philipp Thies:** Investigation, Validation. **Johanning Lars:** Writing – original draft, Reviewing, Editing. **James Cowles:** Writing – original draft, Reviewing, Editing.

Declaration of competing interest

The authors declare that they have no known competing financial interests or personal relationships that could have appeared to influence the work reported in this paper.

Acknowledgements

This study has received funding through the project "Autonomous Robotic Intervention System For Extreme Maritime Environments (ARISE) Stage 2″, as part of the Industry Strategy Challenge Fund (ISFC) funded by Innovate U.K. (UKRI), Project Reference: 104831. The support through Orcina through the provision of their Orcaflex software also kindly acknowledged. The second author would also like to acknowledge funding through the EPSRC Supergen ORE Hub [EP/S000747/1].

References

Ablow, C., Schechter, S., 1983. Numerical simulation of undersea cable dynamics. Ocean. Eng. 10 (6), 443–457.
Alvarez, A., Bertram, V., Gualdesi, L., 2009. Hull hydrodynamic optimization of autonomous underwater vehicles operating at snorkeling depth. Ocean. Eng. 36 (1), 105–112.
Anderlini, E., Parker, G.G., Thomas, G., 2018. Control of a ROV carrying an object. Ocean. Eng. 165, 307–318.
Bertram, V., 2008. Unmanned Surface Vehicles-A Survey, vol. 1. Skibsteknisk Selskab, Copenhagen, Denmark, pp. 1–14.
Bonaschi, G.A., Filatova, O., Mercuri, C., Muntean, A., Peletier, M.A., Shchetnikava, V., Siero, E., Zisis, I., 2012. Identification of a Response Amplitude Operator for Ships.
Bruno, F., Muzzupappa, M., Lagudi, A., Gallo, A., Spadafora, F., Ritacco, G., Angilica, A., Barbieri, L., Di Lecce, N., Saviozzi, G., 2015. A ROV for Supporting the Planned Maintenance in Underwater Archaeological Sites, Oceans 2015-Genova. IEEE, pp. 1–7.
Capocci, R., Dooly, G., Omerdić, E., Coleman, J., Newe, T., Toal, D., 2017. Inspection-class remotely operated vehicles—a review. J. Mar. Sci. Eng. 5 (1), 13.
Chin, C., Lau, M., 2012. Modeling and testing of hydrodynamic damping model for a complex-shaped remotely-operated vehicle for control. J. Mar. Sci. Appl. 11 (2), 150–163.
Christ, R.D., Wernli Sr, R.L., 2011. The ROV Manual: a User Guide for Observation Class Remotely Operated Vehicles. Elsevier.
Conte, G., Scaradozzi, D., Mannocchi, D., Ciuccoli, N., 2017. Field test of an integrated ASV/ROV platform. In: The 27th International Ocean and Polar Engineering Conference. International Society of Offshore and Polar Engineers.
Cristi, R., Papoulias, F.A., Healey, A.J., 1990. Adaptive sliding mode control of autonomous underwater vehicles in the dive plane. IEEE J. Ocean. Eng. 15 (3), 152–160.
Cummins, W., 1962. The Impulse Response Function and Ship Motions. David Taylor Model Basin, Washington DC.
Eidsvik, O.A., 2015. Identification of Hydrodynamic Parameters for Remotely Operated Vehicles, Master's Thesis. NTNU.
Falnes, J., Kurniawan, A., 2020. Ocean Waves and Oscillating Systems: Linear Interactions Including Wave-Energy Extraction. Cambridge university press.
Fang, M.-C., Hou, C.-S., Luo, J.-H., 2007. On the motions of the underwater remotely operated vehicle with the umbilical cable effect. Ocean. Eng. 34 (8–9), 1275–1289.
Feng, Z., Allen, R., 2004. Evaluation of the effects of the communication cable on the dynamics of an underwater flight vehicle. Ocean. Eng. 31 (8–9), 1019–1035.
Ferreira, H., Martins, A., Dias, A., Almeida, C., Almeida, J.M., Silva, E.P., 2007. Roaz Autonomous Surface Vehicle Design and Implementation. Robótica Controlo, Automação, instrumentação.
Field, A., Cherchas, D., Calisal, S., 2000. Optimal Control of an Autonomous Underwater Vehicle. World Automatic Congress.
Fossen, T.I., 1999. Guidance and Control of Ocean Vehicles. University of Trondheim, Norway, Printed. John Wiley & Sons, Chichester, England, ISBN 0 471 94113 1. Doctors Thesis.
Frost, A., McMaster, A., Saunders, K., Lee, S., 1996. The development of a remotely operated vehicle (ROV) for aquaculture. Aquacult. Eng. 15 (6), 461–483.
Greco, M., Colicchio, G., Faltinsen, O., 2009. Bottom slamming for a very large floating structure: uncoupled global and slamming analyses. J. Fluid Struct. 25 (2), 406–419.
Healey, A.J., Lienard, D., 1993. Multivariable sliding mode control for autonomous diving and steering of unmanned underwater vehicles. IEEE J. Ocean. Eng. 18 (3), 327–339.
Healey, A.J., Marco, D., 1992. Slow speed flight control of autonomous underwater vehicles: experimental results with NPS AUV II. In: The Second International Offshore and Polar Engineering Conference. International Society of Offshore and Polar Engineers.
Julca Avila, J., Nishimoto, K., Mueller Sampaio, C., Adamowski, J.C., 2012. Experimental investigation of the hydrodynamic coefficients of a remotely operated vehicle using a planar motion mechanism. J. Offshore Mech. Arctic Eng. 134 (2).
Kim, J., Yu, S.-C., 2016. Convolutional Neural Network-Based Real-Time ROV Detection Using Forward-Looking Sonar Image, 2016 IEEE/OES Autonomous Underwater Vehicles (AUV). IEEE, pp. 396–400.
Kumar, A., Kurmi, J., 2018. A REVIEW ON unmanned water surface vehicle. Int. J. Adv. Res. Comput. Sci. 9 (Special Issue 2), 95.
L3Harris, 2020. C-Worker 7. https://www.asvglobal.com/product/c-worker-7/.
Li, J.-H., Lee, P.-M., 2005. Design of an adaptive nonlinear controller for depth control of an autonomous underwater vehicle. Ocean. Eng. 32 (17–18), 2165–2181.
Pastore, T., Djapic, V., 2010. Improving autonomy and control of autonomous surface vehicles in port protection and mine countermeasure scenarios. J. Field Robot. 27 (6), 903–914.
Roberts, G.N., Sutton, R. (Eds.), 2006. Advances in Unmanned Marine Vehicles, IEE Control Engineering Series. ISBN 10 0863414508.
Sager, W., Shyu, J., Manley, J., 2008. Exploring the west Florida escarpment with high resolution geophysical sonar. Sea Technol. 49 (6).
Seaeye, S., 2020. Falcon. https://www.saabseaeye.com/index.php/solutions/underwater-vehicles/falcon.
Sivčev, S., Coleman, J., Omerdić, E., Dooly, G., Toal, D., 2018. Underwater manipulators: a review. Ocean Eng. 163, 431–450.
Švec, P., Thakur, A., Raboin, E., Shah, B.C., Gupta, S.K., 2014. Target following with motion prediction for unmanned surface vehicle operating in cluttered environments. Aut. Robots 36 (4), 383–405.
Trslic, P., Rossi, M., Robinson, L., O'Donnel, C.W., Weir, A., Coleman, J., Riordan, J., Omerdic, E., Dooly, G., Toal, D., 2020. Vision based autonomous docking for work class ROVs. Ocean. Eng. 196, 106840.
Yan, R.-j., Pang, S., Sun, H.-b., Pang, Y.-j., 2010. Development and missions of unmanned surface vehicle. J. Mar. Sci. Appl. 9 (4), 451–457.
Yu, Z., Shen, Y., Amdahl, J., Greco, M., 2016. Implementation of linear potential-flow theory in the 6DOF coupled simulation of ship collision and grounding accidents. J. Ship Res. 60 (3), 119–144.
Zhao, C., Thies, P., Johanning, L., Tobin, S., 2020. Modelling and Assessment of ROV Capacity within an Autonomous Offshore Intervention System.
Zhu, K.-q., Zhu, H.-y., Zhang, Y.-s., Jie, G., Miao, G.-p., 2008. A multi-body space-coupled motion simulation for a deep-sea tethered remotely operated vehicle. J Hydrodynamics, Ser. B 20 (2), 210–215.